Relaxations around the substitutional chromium site in emerald: X-ray absorption experiments and density functional calculations

Emilie Gaudry,[1] Delphine Cabaret,[2] Christian Brouder,[2] Isabelle Letard,[3] Andreï Rogalev,[3] Fabrice Wilhlem,[3] Nicolas Jaouen,[4] and Philippe Sainctavit[2]

[1]*LSG2M, UMR CNRS 7584, Institut National Polytechnique de Lorraine, Ecole des Mines de Nancy, Parc de Saurupt, F-54042 Nancy Cedex, France*

[2]*IMPMC UMR CNRS 7590, Université Pierre et Marie Curie—Paris 6, Campus Boucicaut, 140 rue de Lourmel, 75015 Paris, France*

[3]*ESRF, Boîte Postale 220, 38043 Grenoble Cedex 9, France*

[4]*Synchrotron SOLEIL, L'Orme des Merisiers Saint-Aubin, Boîte Postale 48, 91192 Gif-sur-Yvette Cedex, France*

(Received 13 April 2007; revised manuscript received 4 July 2007; published 18 September 2007)

We determine the local crystallographic and electronic structure around the chromium impurity in emerald (a chromium doped beryl) by combining *ab initio* density functional calculations and x-ray absorption experiments in both x-ray absorption near edge structure (XANES) and extended x-ray absorption fine structure (EXAFS) regions. The isotropic and natural linear dichroic signals at the Cr *K* edge have been recorded using single crystals and a reliable method has been applied to remove diffraction peaks. The contributions of both electric dipolar and electric quadrupolar transitions in the XANES preedge are calculated and analyzed within group theory. This study reveals that the introduction of chromium in beryl leads to relaxations that are mainly local. The oxygen atoms in the coordination shell relax to a bond distance similar to that for Cr in ruby (α-Al_2O_3:Cr^{3+}). Angular relaxations are found to affect essentially the chromium first neighbors.

DOI: 10.1103/PhysRevB.76.094110 PACS number(s): 78.70.Dm, 82.33.Pt, 71.15.Mb, 61.72.Bb

I. INTRODUCTION

Beryls are popular gems, partly because they present a large panel of magnificent colors. Pure beryl ($Be_3Si_6Al_2O_{18}$), also called goshenite, is a colorless mineral. However, beryls are able to store various foreign substances in their structure, and this gives rise to the various colors: morganites ($Be_3Si_6Al_2O_{18}$:Mn) are rose, heliodores ($Be_3Si_6Al_2O_{18}$:Fe,U) are yellow, aquamarines ($Be_3Si_6Al_2O_{18}$:Fe) are blue, and emeralds ($Be_3Si_6Al_2O_{18}$:Cr or $Be_3Si_6Al_2O_{18}$:V) are green. The colors of these minerals are generally interpreted within the ligand field theory. This model is based on an electrostatic interaction between the dopant cation and the ligands of its coordination sphere. Since the color of a doped crystal is linked to the position of the absorption bands of the doping cation within the host gap, it depends on the crystal field parameter $10Dq$ which is related to the impurity-ligand distance within various theories such as the point charge model. The color diversity in minerals doped with the same impurity is then often explained by a change of the local environment around the dopant cation. For example, the difference of color between red ruby (α-Al_2O_3:Cr^{3+}) and green chromic emerald ($Be_3Si_6Al_2O_{18}$:Cr^{3+}), which are both doped by chromium in the same valence state and in a similar octahedral environment made by six oxygen atoms, is attributed to a supposed weaker and longer Cr-O bonding in emerald than in ruby.[1–3] To check this argument, a precise description of the local environment around chromium in green emerald ($Be_3Si_6Al_2O_{18}$:Cr^{3+}) is needed since the local environment around chromium in red ruby (α-Al_2O_3:Cr^{3+}) has been described.[4–6]

Many techniques have been used to show the existence of structural relaxations around impurities in minerals: UV-visible spectroscopy,[7,8] electron paramagnetic resonance spectroscopy,[9,10] single crystal x-ray diffraction.[11,12] However, these techniques are inaccurate when it comes to determine precisely the distances between the impurity and the neighboring ligands. X-ray absorption spectroscopy (XAS) is a powerful technique in order to measure these distances since the selectivity of the XAS allows to probe the environment of one particular element. In the case of dilute ions in single crystals, collecting the XAS spectra with a good signal-to-noise ratio is a difficult task: the diffraction peaks due to the host crystal strongly distort the absorption signal,[13] the worst case being met for the lower concentrations of the impurity. Extended x-ray absorption fine structure (EXAFS) has been successfully applied to determine the two Cr-O bond lengths of the coordination shell of the chromium impurity in ruby and the two Fe-O bond lengths of the coordination shell of the iron impurity in doped sapphire.[4] Given that x-ray absorption near edge structure (XANES) is sensitive to small variations in interatomic distances within the coordination shell of the absorbing atom,[5] it is then possible to check the validity of a structural model for the local environment around the impurity atom in the sample. In addition to the experimental difficulties to collect good XAS spectra, obtaining microscopic information from *ab initio* calculations is not trivial: this requires the use of large supercells to account for the low concentration of impurity atoms. All these reasons explain why the local crystallographic structure around impurities is unknown in most cases.[5,14,15]

In this paper, we investigate the local crystallographic and electronic structures around green chromic emeralds ($Be_3Si_6Al_2O_{18}$:Cr^{3+}) for which the color is due to the presence of Cr^{3+} ions in the beryl structure ($Be_3Si_6Al_2O_{18}$). To examine the local environment around chromium, we combine both XAS experiments at the Cr *K* edge of two samples (one natural emerald and one synthetic emerald) and theoretical *ab initio* calculations. Diffraction peaks on the EXAFS

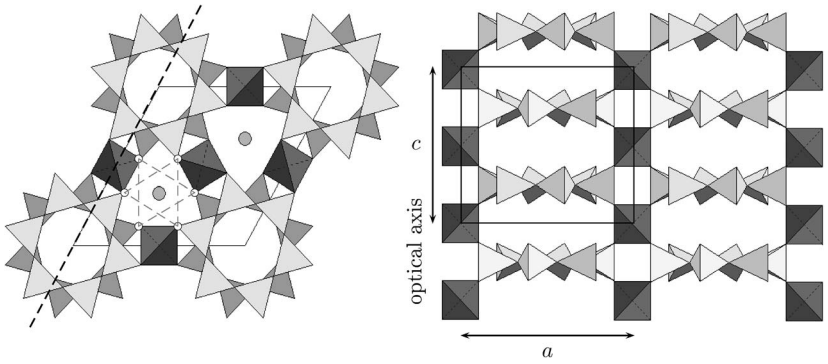

FIG. 1. Beryl structure projected in a plane perpendicular to the optical axis (left) or parallel to the optical axis (right). The black tetrahedra contain the beryllium atoms, and the dark gray and light gray tetrahedra contain the silicon atoms. The aluminum atoms are the gray circles. The white circles around one of the aluminum atom (left) represent the oxygen atoms of its coordination shell (the octahedral site is shown by the gray dashed line). The unit cell is denoted by a black line. The dashed line in the left part of the figure describes the plane used to obtain the right part of the figure.

signal are eliminated by the same method as the one described before,[4] and we introduce in this paper a more efficient scheme to treat the XANES spectra. XANES spectra provide both structural and electronic information up to the medium range order. Due to the photoelectron multiple scattering in the XANES region, the analysis of the XANES spectra requires a sophisticated theoretical development. In many cases, a more empirical fingerprint approach is preferred in order to determine the site geometry and the valence of the absorbing atom.[16–18] However, extracting precise structural and electronic information is only possible through simulations. An efficient first-principles approach based on plane-wave pseudopotential formalism has been developed to calculate *K*-edge XANES spectra.[19] Here, we apply this method to the Cr *K* edge in green emeralds. The x-ray-matter interaction is taken into account with both electric dipole and electric quadrupole terms. Information about the electronic structure around the chromium impurity atom is provided by the fine analysis of the *K* preedge, which is the sum of contributions from $1s \rightarrow p$ electric dipole transitions and $1s \rightarrow d$ electric quadrupole transitions.

This paper is organized as follows. Section II is dedicated to the methods, including the sample description (Sec. II A), the x-ray absorption measurements (Sec. II B), and the calculation framework (Sec. II C). Section III is devoted to the results and discussion. We first present the structural model imaging the relaxations around chromium in emerald based on our theoretical and empirical findings (Sec. III A). Then, the electronic structure of chromium in emerald is probed through the *K*-edge and preedge analysis (Sec. III B). Section IV summarizes the conclusions of this study.

II. MATERIALS, EXPERIMENTS, AND ANALYSIS METHODS

A. Crystallographic structure of beryl ($Be_3Si_6Al_2O_{18}$) and sample description

Beryl belongs to the $P6/mcc$ (D_{6h}^2) space group.[20–22] The hexagonal unit cell contains two $Be_3Si_6Al_2O_{18}$ species (Fig. 1). Beryl is a cyclosilicate, where six SiO_4 tetrahedra of the structure are linked together to form a ring.[23] The Si_6O_{18} rings lie one above the others to build canals parallel to the optical axis of the sample. The atomic site of aluminum is a distorted octahedron made by six oxygen atoms with a 3.2 (D_3) local point symmetry. The atomic site of beryllium is a distorted tetrahedral site made by four oxygen atoms, with a 222 (D_2) local point symmetry. The unit cell contains two types of oxygen atoms: 12 of them are shared between SiO_4 tetrahedra within the rings and 24 of them link SiO_4 tetrahedra to BeO_4 tetrahedra or to AlO_6 octahedra. The size of the unit cell varies with the exact chemical composition (impurity concentration) of the analyzed sample. The *c* parameter varies from 9.10 to 9.25 Å and the *a* parameter from 9.15 to 9.52 Å. The *a* parameter is close to the *c* parameter: the ratio $\frac{c}{a}$ varies from 0.98 to 1.03. The values of *a* and *c* parameters for synthetic materials are given by Refs. 24 and 25. For beryl, the cell parameters are $a=9.21_2\pm0.00_4$ Å and $c=9.18_7\pm0.00_6$ Å. For emerald, the cell parameters are $a=9.21_9\pm0.00_1$ Å and $c=9.19_8\pm0.00_1$ Å.

Two single crystals of doped beryl have been used for this study: a synthetic sample, obtained by hydrothermal synthesis, containing only chromium impurities (around 1200 ppm), and a natural sample, containing chromium, vanadium, and iron impurities (around 200 ppm for each type of impurity). These compositions were analyzed using the Cameca microbeam electron microprobe at the CAMPARIS analytical facility of the Universities of Paris 6/7. A 20 kV acceleration with a 15 nA beam current, defocused to 10 μm, was used. X-ray intensities were corrected for dead-time, background, and matrix effects using the Cameca ZAF (atomic number absorption fluorescence) routine. The standards used were α-Cr_2O_3, α-Fe_2O_3, and V_2O_5. The synthetic sample has an oblong shape (about 15 mm long by 5 mm large). The longer side is parallel to the optical axis of the crystal. The natural sample has the characteristic shape of beryl crystals (a cylinder with a hexagonal basis). The optical axis is the cylinder axis.

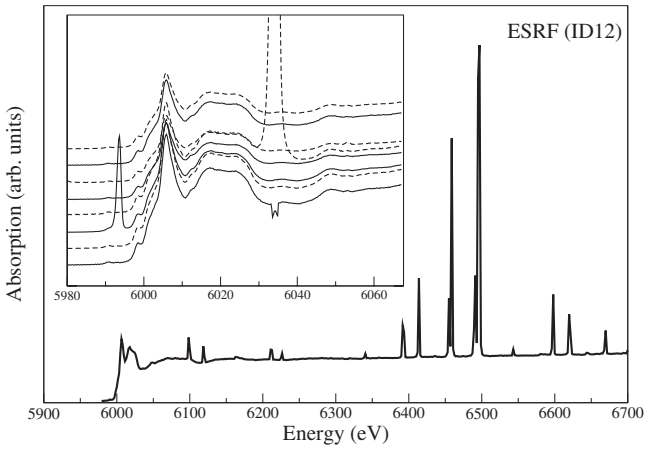

FIG. 2. Cr K edge in emerald ($Be_3Si_6Al_2O_{18}:Cr^{3+}$). The EXAFS spectra are collected with the optical axis of the sample parallel to the polarization of x ray (it is the average spectra collected with the eight detectors). The XANES spectra (inset) are collected for $\theta=-\frac{\pi}{6}$, where θ is the angle between the optical axis of the sample and the polarization of x ray. The contributions of the eight detectors are outlined.

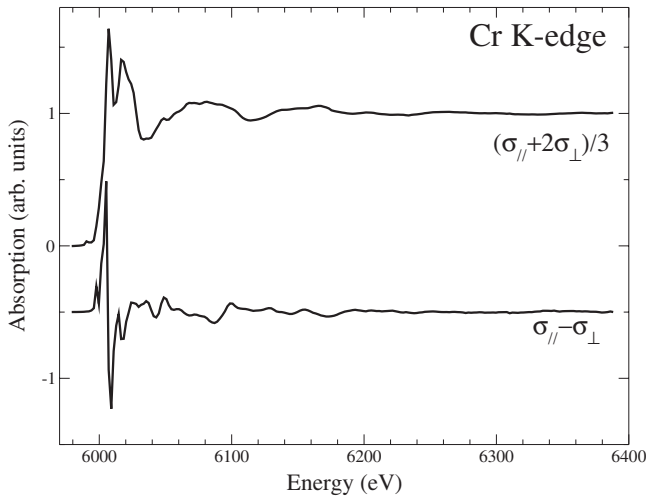

FIG. 3. EXAFS isotropic $\left(\frac{\sigma_{\parallel}+2\sigma_{\perp}}{3}\right)$ and dichroic $(\sigma_{\parallel}-\sigma_{\perp})$ spectra at the Cr K edge in the synthetic emerald ($Be_3Si_6Al_2O_{18}:Cr^{3+}$).

B. X-ray absorption measurements and analysis

1. X-ray absorption measurements

The chromium K edges (energy range: 5900–6400 eV) in both emeralds have been measured on the ID12 beamline of the European Synchrotron Radiation Facility (ESRF, France) dedicated to polarization dependent spectroscopies.[26–28] The monochromatic x-ray beam is obtained through a double Si(111) crystal monochromator, having a resolution $\Delta E/E \sim 10^{-4}$. The data were collected by total fluorescence yield detection. No reabsorption correction was necessary since the chromium concentration in the samples is low (around 1200 ppm for the synthetic crystal and around 200 ppm for the natural emerald).

In doing XAFS measurements on single crystals, one is faced with the problem of very intense diffraction peaks. These arise from either diffracted rays striking a fluorescence detector or from the occurrence of diffraction inside the crystal.[13] These diffraction rays are broad and have devastating effects on the whole absorption spectrum. In order to decrease the intensity of diffraction peaks and elastic scattering, a vanadium filter is used. Despite the fact that the diffracted intensity is greatly reduced, it is still present (see Fig. 2) and it can be fully eliminated by the use of the following technique. The ID12 beamline is equipped with a rotating holder, which rotation axis is aligned parallel to the propagation vector of the x ray. Each oriented sample is mounted on this rotating holder so that its optical axis stays perpendicular to the x-ray propagation vector when the holder is turned. In doing so, the angle between the optical axis of the sample and the linear polarization of x ray can be varied from 0 to 2π rad. At each energy point of the spectrum, the cross section is measured for a series of angles between the optical axis and the polarization vector. This process is carried out for each energy point of the EXAFS or XANES energy range (the energy step is about 0.2 eV for the XANES region and 2.0 eV for the EXAFS region). Then, the isotropic and the natural linear dichroism EXAFS and XANES signals have to be extracted from a large amount of data. We denote by $\sigma_{\parallel}$ the absorption cross section obtained for the x-ray polarization parallel to the optical axis of the sample and by $\sigma_{\perp}$ the absorption cross section obtained for the x-ray polarization perpendicular to the optical axis of the sample. In the electric dipole approximation, the isotropic cross section is then given by $\frac{\sigma_{\parallel}+2\sigma_{\perp}}{3}$ and the natural linear dichroic signal by $\sigma_{\parallel}-\sigma_{\perp}$.

A filtering algorithm detailed in Refs. 4 and 29 is used to obtain, simultaneously, both the isotropic absorption coefficient and the natural linear dichroic EXAFS signal (see Fig. 3). This method is used to eliminate diffraction peaks in EXAFS spectra and requires a huge beam time since EXAFS spectra have to be recorded for 150 values of the angle θ between the polarization of x ray and the optical axis of the sample. Obviously, it would be identical to get the XANES spectra by using the same method. However, to obtain the XANES signal at the Cr K edge of the emerald samples, we applied a faster and more efficient method which required the registration of the spectra for only about ten values of the angle θ. This data analysis method which uses the angular dependence of the EXAFS spectra determined before is described in the following.

The procedure to extract the XANES $\sigma_{\parallel}$ and $\sigma_{\perp}$ cross sections from the experimental data consists of several steps. (i) For each angle θ_k and each detector ℓ $(1 \leqslant \ell \leqslant 8)$, the main diffraction peaks of the experimental spectra $Y(\ell, \theta_k, E_i)$ are eliminated by removing the data points i such that $[Y(\ell, \theta_k, E_{i+1}) - Y(\ell, \theta_k, E_i)]/(E_{i+1} - E_i)$ is larger than a threshold η. This procedure is used for energies beyond 6032 eV with $\eta=0.005$. (ii) The same procedure was repeated with a threshold $\eta=0.01$. (iii) To remove the remaining diffraction peaks for each angle θ_k and each detector ℓ, the XANES data $Y(\ell, \theta_k, E_i)$ are first fitted to the EXAFS

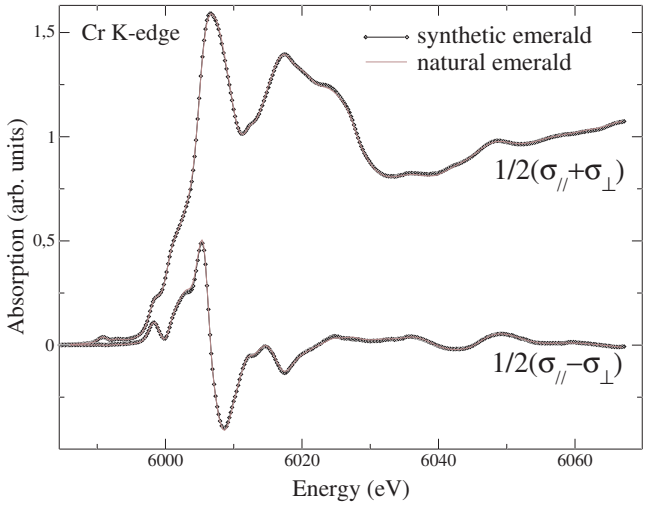

FIG. 4. (Color online) XANES spectra at the Cr *K* edge of emerald ($Be_3Si_6Al_2O_{18}:Cr^{3+}$). The spectra collected with the synthetic sample and the natural sample are superimposed.

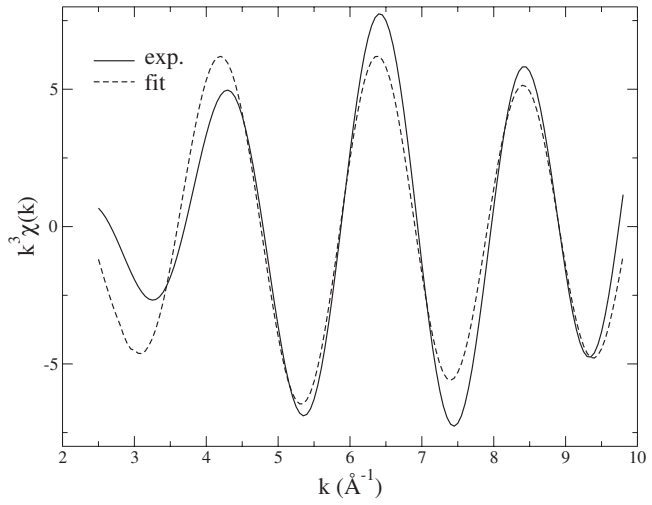

FIG. 5. Fit of the isotropic EXAFS signal at the Cr *K* edge in emerald ($Be_3Si_6Al_2O_{18}:Cr^{3+}$). Four adjustable parameters are fitted for the chromium coordination shell: $r_{Cr\text{-}O}=1.97_5\pm0.00_5$ Å, $\sigma_O=0.056\pm0.01_0$ Å, $N_O=4.7\pm1.0$, and $\Delta E_O=-0.47\pm1.00$ eV (see text for explanations of the fitting parameters).

data $Y_e(\theta_k,E_i)$ by the equation

$$Y_e(\theta_k,E_i)=aY(\ell,\theta_k,E_i)+bE_i+c;$$

the terms bE_i+c were used to normalize the spectra and remove possible drifts, but they were found negligible thanks to the high stability of the ID12 beamline. Let σ^{rms} be the rms error of the fit and let σ_i^{rms} be the rms error of the fit when point E_i is removed from the data. The difference $|\sigma^{rms}-\sigma_i^{rms}|$ is calculated for all E_i and takes its maximum value for a given point E_j. If $|\sigma_j^{rms}-\sigma^{rms}|/\sigma_j^{rms}$ is larger than a threshold η' (here $\eta'=0.00_5$), then point E_j is removed from the data. This procedure is repeated until no point is removed. (iv) For each angle θ_k, the data points that were not eliminated by the previous procedure are then averaged over the eight detectors, giving $Y(\theta_k,E_i)$. This gives us experimental spectra without diffraction peaks but with small "glitches." (v) The remaining glitches are removed by fitting σ_1 and σ_2 to the spectra $Y(\theta_k,E_i)$ through the equation $Y(\theta_k,E_i)=\sigma_1(E_i)+\sigma_2(E_i)\cos(2\theta_k+\phi)$. In our example, $k=1,\ldots,12$. The XANES $\sigma_\parallel$ and $\sigma_\perp$ cross sections are then deduced from σ_1, σ_2, and ϕ. The result of this procedure is shown in Fig. 4 for synthetic and natural emeralds. For more details and pictures of the spectra obtained after each step, see Ref. 30.

2. Extended x-ray absorption fine structure analysis

The EXAFS signals at the Cr *K* edge are analyzed by two complementary methods. The first method is the shell by shell analysis: the contributions from neighboring atoms of chromium in emerald are analyzed by a Fourier series of plane wavelets. As a second method, we applied a whole range simulation of $k^3\chi(k)$ using structural models and calculations of the Cr *K* edge. This simulation technique is described below.

For the shell by shell analysis, a standard procedure is used to analyze the isotropic part of the two absorption spectra.[31,32] The preedge background is removed by applying a polynomial fit to the preedge data and extrapolating it into the postedge region. Data normalization and energy shift are performed using an error function (step function) and a pseudo-Voigt function (peak function). The energy scale is converted to reciprocal space units. Then, a cubic spline function is fitted to the k^3 weighted data by a nonlinear least squares fit of the spline knots. These normalized EXAFS signals $\chi(k)$ are further analyzed as a Fourier series of plane wavelets.[33] The *k* range used to obtain the radial structure function in real space is from 2.45 to 9.85 $Å^{-1}$. An appropriate *r* range is selected to separate the contributions of the nearest shells from the total experimental signal using back Fourier transform. Typically, the *r* range is from 0.98 to 2.95 Å. EXAFS fitting was performed using the program EXAFS[32] with theoretical phases, amplitudes, and mean free paths calculated with a real space multiple scattering approach for a muffin-tin potential with a screened core hole[34] implemented in the FEFF8 code.[35] The structural model is obtained by the method described in Sec. II C 1. Four adjustable parameters were fitted for the chromium coordination shell (Fig. 5): they are (i) the Cr-O distance ($r_{Cr\text{-}O}=1.97_5\pm0.00_5$ Å), (ii) the Debye-Waller factor ($\sigma_O=0.056\pm0.01_0$ Å) that accounts for structural disorder and thermal vibration, (iii) the number of oxygen neighbors ($N_O=4.7\pm1.0$), and the phenomenological parameter ΔE ($\Delta E_O=-0.47\pm1.00$ eV) that corrects the phase functions.[36]

For the global simulation of the EXAFS spectra, the FEFF8 code is used in order to calculate the $k^3\chi(k)$ signal using the structural model obtained by *ab initio* energy minimization and described in Sec. II C 1. This calculated spectra are then compared to the experimental one (Fig. 6). The agreement is fair between the calculated spectra (for both isotropic and dichroic signals) and the corresponding experimental spectra. It is to be kept in mind that there is no fitting procedure and that the calculated spectra are directly connected to the *ab initio* relaxation calculation.

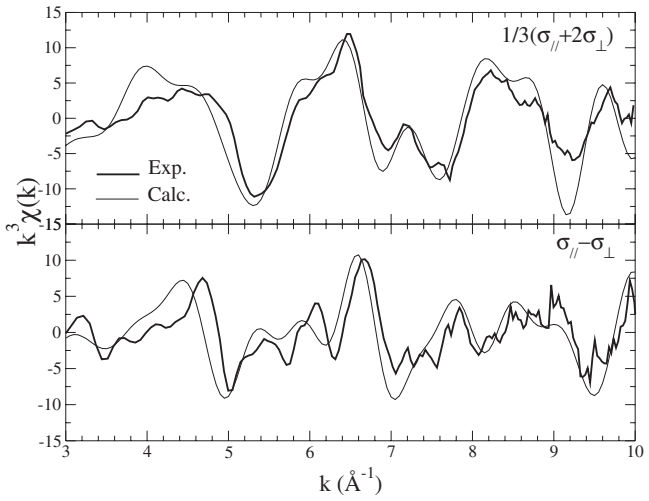

FIG. 6. Comparison of the experimental and FEFF-calculated EXAFS $k^3\chi(k)$ isotropic $\left(\frac{\sigma_{\parallel}+2\sigma_{\perp}}{3}\right)$ and dichroic $(\sigma_{\parallel}-\sigma_{\perp})$ signals.

C. Computational methods

1. Structural model construction

The starting point of any calculation allowing a precise analysis of x-ray absorption spectra is a structural model. The structural model for emerald ($Be_3Si_6Al_2O_{18}$:Cr^{3+}) is obtained by *ab initio* energy minimization calculation of the beryl structure ($Be_3Si_6Al_2O_{18}$) with one aluminum atom substituted for one chromium atom. The calculation code used is the Car-Parrinello molecular dynamics with simulated annealing[37,38] as implemented in the CPMD code.[39] This code is based on the density functional theory (DFT) within the local spin-polarized density approximation (LSDA) with the parametrization of Ref. 40. The atomic cores are described by norm-conserving pseudopotentials in the Kleinman-Bylander form.[41,42]

The starting structure for the energy minimization calculation is a hexagonal cell built on the vectors $\vec{a}_H$, $\vec{b}_H$, $\vec{c}_H$. It contains 58 atoms: 1 chromium atom and 3 aluminum atoms at the 4*c* position (Wyckoff notation) of the *P*6/*mcc* space group, 6 beryllium atoms (6*f* position), 12 silicon atoms (12*l* position), and 36 oxygen atoms (12*l* and 24*m* positions). The lattice parameters used are $a_H=b_H=9.21$ Å and $c_H=9.19$ Å. The *x*, *y*, *z* values determining the starting positions of the Si and O atoms are given by Ref. 25. All atom coordinates are free to relax, while the lattice constants are fixed: the chromium concentration is estimated to be low enough (1.7 at. %) not to modify the mean cell parameter. Since the starting atomic positions are those of beryl, the symmetry of the trivalent ion site is D_3 at the beginning of the calculation. During the relaxation process, this symmetry is let free to relax, but it was found that this D_3 symmetry is preserved at the end of the calculation. Similar results concerning the symmetry conservation were observed in doped α-Al_2O_3 around trivalent iron, titanium, and chromium ions.[5]

The chromium impurity is known to be in its high-spin state,[43] then the spin multiplet $S_z=\frac{3}{2}$ for the unit cell is imposed (the electronic configuration of Cr^{3+} is $[Ar]4s^03d^3$). The parametrization of the norm-conserving Troullier-Martins pseudopotentials is given in Table I. The wave functions and the charge density are extended in plane waves with an 80 and a 320 Ry cutoff, respectively. The Brillouin zone was sampled at the Γ point. At the end of the *ab initio* energy minimization, it has been checked that the forces between atoms were less than 26 meV/Å (i.e., 10^{-3} Ry/a.u.).

2. X-ray absorption near edge structure simulations

The analysis of the experimental XANES data is not straightforward. *Ab initio* XANES simulations are required to relate the experimental spectra features to the local structure around the absorbing atom.

The XANES calculations are performed within an *ab initio* total energy code[44] using the formalism described in Refs. 19 and 45. This code is based on DFT within LSDA and uses a plane-wave basis set and norm-conserving Troullier-Martins pseudopotential in the Kleiman-Bylander form.[41,42] The all-electron wave functions are reconstructed within the projector augmented wave framework.[46] In order to allow the treatment of large systems, the scheme uses a recursion method to construct a Lanczos basis and then compute the cross section as a continued fraction,[47,48] in both electric dipole and electric quadrupole approximations.

XANES spectra are calculated using the structural model resulting from *ab initio* energy minimization. The pseudopotentials are generated using the parametrization given in Table I. In order to account for the core-hole effects in the calculation, the Cr pseudopotential is obtained with only one 1*s* electron. The spin multiplet degeneracy is set by imposing the number of up and down states given by the CPMD code $\left(S_z=\frac{3}{2}\right)$. Convergence of the XANES theoretical spectra is reached for the following set of parameters: an 80 Ry energy cutoff, one *k* point for the self-consistent spin-polarized

TABLE I. Parameters used to generate the norm-conserving pseudopotentials. The core radii of the valence states are indicated in brackets in Å.

Atom	Al	O	Cr	Be	Si
Valence states	3*s* (1.06)	2*s* (0.77)	3*s* (0.53)	2*s* (1.06)	3*s* (1.06)
	3*p* (1.06)	2*p* (0.77)	3*p* (0.90)	2*p* (1.06)	3*p* (1.06)
	3*d* (1.06)		3*d* (0.90)		3*d* (1.06)
Electronic configuration	$3s^23p^03d^0$	$2s^22p^4$	$3s^23p^63d^3$	$2s^{0.2}2p^0$	$3s^23p^13d^{0.5}$
Local part	*d*	*p*	*d*	*p*	*d*

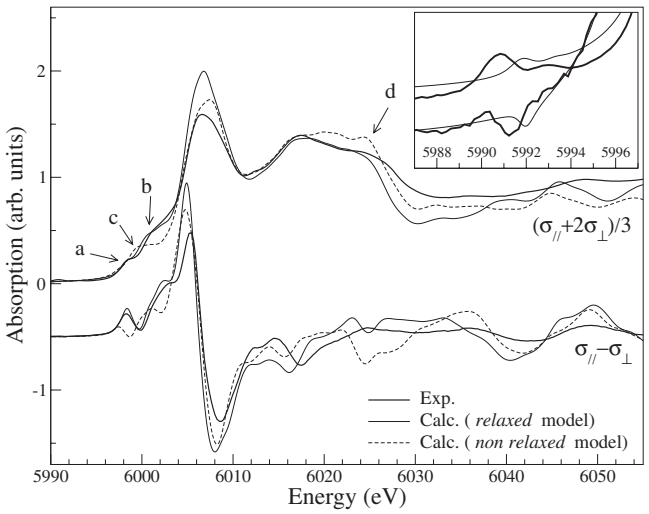

FIG. 7. Isotropic $\left(\frac{\sigma_{\parallel}+2\sigma_{\perp}}{3}\right)$ and dichroic $(\sigma_{\parallel}-\sigma_{\perp})$ XANES spectra collected at the Cr *K* edge in emerald ($Be_3Si_6Al_2O_{18}:Cr^{3+}$). The experimental signal (thick line) is compared with the calculations made from the *relaxed* structural model (straight line) and from the *nonrelaxed* structural model (dotted line). Inset: zoom of the preedge region.

charge density calculation, and a Monkhorst-Pack grid of $4\times4\times4$ *k* points in the Brillouin zone[49] for the absorption cross-section calculation. An energy-dependent broadening parameter γ is used in the continued fraction in order to account for the two main photoelectron damping modes.[50] The energy-dependent parameter γ used in this study is the one described in Ref. 5. Isotropic and dichroic calculated spectra are shown in Fig. 7.

III. RESULTS AND DISCUSSION

Our main goal is to determine precisely the local structure around chromium in emerald. To do so, we have analyzed various sets of experimental data (isotropic and dichroic EXAFS and XANES spectra) and performed density functional calculations. The comparison of the results given by all these techniques allows a reliable description of the chromium site in emerald. Before going further in the discussion, we should notice that both the isotropic and the dichroic XANES spectra of the natural crystal and of the synthetic emerald are identical (see Fig. 4). It means that the chromium environment is the same in these two samples. The presence of the other impurity elements in the natural emerald seems not to modify the local crystallographic and electronic structures around chromium. This is consistent with the very low concentration of impurities in the sample: the impurity atoms do not gather by pairs. This behavior of the impurity atoms in the natural emerald is then different from what could occur in blue sapphires (α-Al_2O_3:Fe-Ti), where the iron and titanium atoms are expected to lie at two adjacent cationic sites.[51]

A. Relaxations around chromium in emerald

Given that the local point symmetry of aluminum in beryl is D_3, the six oxygen atoms of the coordination shell of the substituting chromium are expected to lie at the same distance from the chromium atom. Furthermore, the angles between the optical axis and each of the six Cr-O bonds are expected to be equal. The analysis of the isotropic EXAFS signal allows to obtain the distances between the chromium atom and its neighboring atoms. The fit of the experimental $k^3\chi(k)$ is shown in Fig. 5. The Cr-O distance found is $1.97_5\pm0.00_5$ Å. It is in agreement with the Cr-O distance obtained by energy minimization calculations (1.99 ± 0.02 Å). The slight difference (0.01_5 Å) between the Cr-O distance from EXAFS analysis and the Cr-O calculated distance might be explained by the already noticed +1% overestimation made by the *ab initio* calculation in these systems.[4] In addition, this DFT calculation indicates that the D_3 symmetry of aluminum in beryl is preserved when chromium is substituted for aluminum. This is also confirmed by the fact that the oxygen shell can be well fitted with one single Cr-O distance. Then, the dichroic signal originates exclusively from the D_3 angular deformation from a pure octahedral coordination and from further neighboring shells.

Further analysis regarding information on atoms beyond the chromium coordination shell is possible with DFT calculation. The chromium-cation bond lengths obtained by the energy minimization calculation in emerald are not so different from the aluminum-cation distances in beryl: the calculated Cr-Be distance in emerald is 2.70 Å (2.66 Å for the calculated Al-Be distance in beryl) and the calculated Cr-Si distance in emerald is 3.31 Å (3.26 Å for the calculated Al-Si distance in beryl). Although the ionic radius of Cr ($r_{Cr^{3+}}=0.61_5$ Å) (Ref. 52) is $\approx$15% larger than the ionic radius of Al ($r_{Al^{3+}}=0.53_5$ Å),[52] the Cr-Be and Cr-Si bond lengths are only less than 2% larger than Al-Be and Al-Si bonds. It seems then that the whole radial relaxation takes place in the coordination shell. This conclusion has been already observed for transition metal impurities and also for heavier elements such as Ta, Cd, and La.[5,14,15,53] In order to evaluate the radial and angular relaxations in emerald, a cluster is obtained from the position of atoms in the supercell given by the DFT calculation, using the method described in Ref. 4. In the supercell, the shortest Cr-Cr distance is 9.2 Å. It is then reasonable to limit any analysis concerning the size of the relaxation around the chromium impurity to a sphere of radius of 4.1 Å. By doing so, relaxations imposed by other impurities are minimized. The norm of the displacement vector of each atom and the variation $\delta\theta=\theta_{\mathrm{unrelax}}-\theta_{\mathrm{relax}}$, where θ_{relax} ($\theta_{\mathrm{unrelax}}$) is the angle between the optical axis and the Cr-atom bond (central Al-atom bond), are shown in Fig. 8. The radial relaxation takes place essentially in the chromium coordination shell (with oxygen atom displacement greater than 0.1 Å). The radial relaxation of the nearest Be and Si cations is not negligible (0.04 Å for Be atoms and 0.03 Å for Si atoms). The radial relaxation of further oxygen atoms is less than 0.03 Å. The angular relaxation in the chromium coordination shell is not negligible since the θ angle varies from 59.5° in beryl to 61.0° in emerald. The Φ angles, defined in Fig. 9 as the shift between the two triangles made by the six oxygen atoms of the chromium coordination shell, are calculated to be 10.8° in beryl and 11.0° in emerald. Further from the central cation, the angular relaxation is small ($\delta\theta$ is

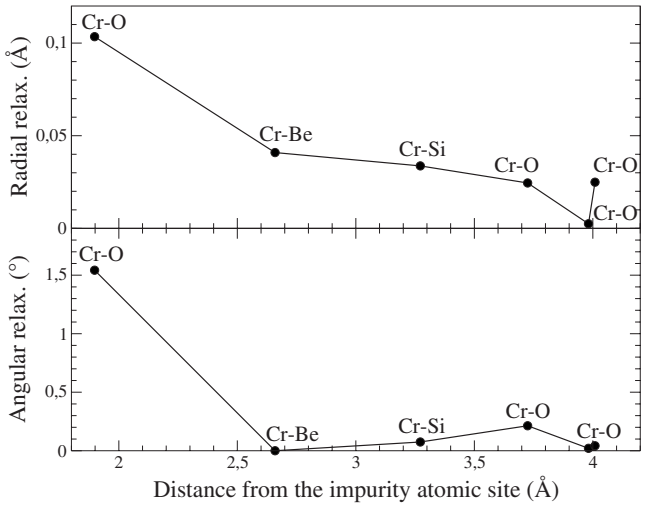

FIG. 8. Radial and angular relaxations around the chromium impurity in emerald. In the upper part, the norms of the displacement vectors of atoms surrounding the central chromium atom are plotted as a function of distance from the impurity. In the lower part, the $\delta\theta$ angle (see text for explanation) is plotted as a function of distance from the impurity.

less than 0.25°). All these calculated data have been summarized in Table II.

The first neighbor distance in emerald ($R_{\text{Cr-O}}=1.97_5$ Å) is found to be greater than the first neighbor distance in beryl ($R_{\text{Al-O}}=1.90_3$ Å) (Refs. 24 and 25) as could be expected from the ionic radius for chromium compared to the ionic radius for aluminum. When comparing the local structures around chromium in emerald and in another chromium doped crystal such as ruby (α-Al_2O_3:Cr^{3+})[4] or doped spinel ($MgAl_2O_4$:Cr^{3+}),[54] one notices that the average Cr-O distances are quite similar: $R_{\text{Cr-O}}=1.96_5$ Å in ruby, $R_{\text{Cr-O}}=1.97_5$ Å in emerald, and $R_{\text{Cr-O}}=1.98$ Å in spinel from EXAFS data analysis. It is not surprising since the mean Al-O distances in the corresponding host crystals are quite the same: $R_{\text{Al-O}}=1.91_5$ Å in ruby,[55] $R_{\text{Al-O}}=1.90_3$ Å in beryl,[24,25] and $R_{\text{Al-O}}=1.93$ Å in $MgAl_2O_4$.[56] This result can also be related to the findings that the Cr-O average distance in the coordination shell is almost independent of the Cr concentration for the solid solution $Al_{2-x}Cr_xO_3$.[6] In addition, given the weak value in ruby (2.6%) and emerald (3.7%) for the ratio $\frac{R_{\text{Cr-O}}-R_{\text{Al-O}}}{R_{\text{Al-O}}}$, ions beyond the coordination sphere are expected to relax slightly in agreement with Ref. 57.

TABLE II. First, second, and third neighbor structural parameters in beryl and emerald. For each shell, the distance from the central cation and the angle θ between the optical axis and the $M-M'$ bond (where M is the central cation and M'=O, Be, or Si) are given. The angle Φ defined as the shift between the two triangles made by the six oxygen atoms of the chromium coordination shell is mentioned. The data result from energy minimization of the beryl structure (column 1) or the chromium doped beryl structure (column 2). The experimental Cr-O distance in emerald is added.

	$Be_3Si_6Al_2O_{18}$	$Be_3Si_6Al_2O_{18}$:Cr^{3+}
Al-O (Å)	1.90	
Cr-O (Å)		1.97_5 (expt.)
		1.99
θ (deg)	59.5	61.0
Φ (deg)	10.8	11.0
Al-Be (Å)	2.66	
Cr-Be (Å)		2.70
θ (deg)	0.0	0.0
Al-Si (Å)	3.26	
Cr-Si (Å)		3.31
θ (deg)	45.4	45.5

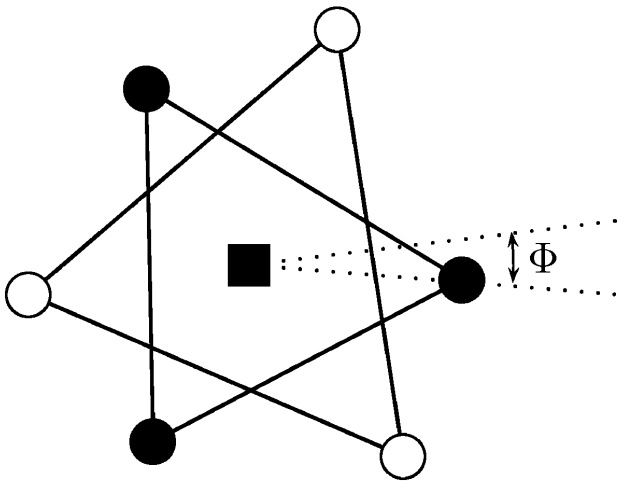

FIG. 9. Projection on the plane Π of the positions of the oxygen atoms lying in the central cation coordination sphere. The Π plane is perpendicular to the optical axis and contains the central atom. The square is the central cation (Al or Cr). The circles are the oxygen anions lying above (white) or below (black) the Π plane.

B. Analysis of the Cr *K* edge

1. Edge features

The isotropic and dichroic EXAFS and XANES spectra calculated using the structural model resulting from *ab initio* energy minimization are in good agreement with the corresponding experimental spectra (Figs. 6 and 7): energy positions and relative intensities of the various *K*-edge features are well reproduced in each case. In the preedge region, both electric dipole ($1s \rightarrow p$) and electric quadrupole ($1s \rightarrow 3d$) transitions occur. An interpretation of this region is detailed in Sec. III B 2. The global shape of the preedge is well reproduced by the calculation (see inset in Fig. 7) but the calculated preedge features are shifted toward higher energies. This may be due to the already noticed[5] limit of the DFT within LSDA to model the core-hole-electron interaction for empty *d* states of 3*d* transition metals.

We have seen in Sec. III A that the relaxation around the chromium impurity is mainly local. Therefore, it is interesting to evaluate the sensitivity of XANES to the subtle structural modifications induced by the introduction of a chro-

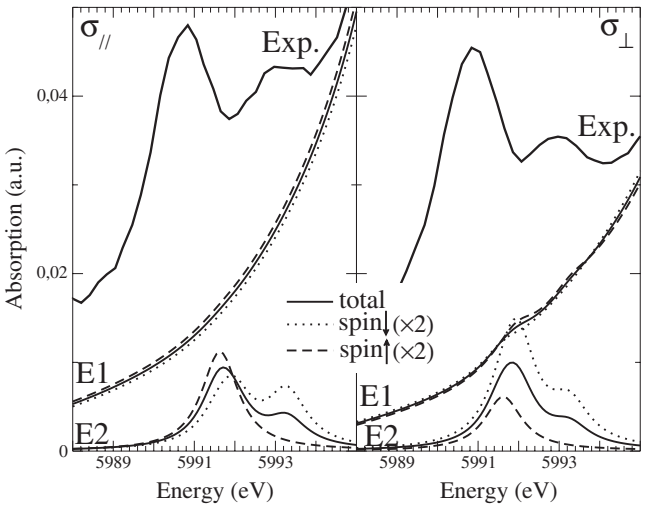

FIG. 10. Left part: XANES preedge spectra collected at the Cr *K* edge in emerald ($Be_3Si_6Al_2O_{18}:Cr^{3+}$) with the x-ray polarization parallel to the optical axis of the sample ($\sigma_{\parallel}$). Right part: XANES preedge spectra collected at the Cr *K* edge in emerald ($Be_3Si_6Al_2O_{18}:Cr^{3+}$) with the x-ray polarization perpendicular to the optical axis of the sample ($\sigma_{\perp}$). The experimental signal (upper spectra) is compared with the simulated signal. The contributions of the dipolar (E1) and the quadrupolar electric (E2) parts are detailed along with the spin up (dashed line) and spin down (dotted line) contributions.

mium impurity in beryl. The calculated XANES spectra using the structural model resulting from *ab initio* energy minimization (called *relaxed* model) are compared with a calculated XANES spectra using another structural model (called *nonrelaxed* model). This nonrelaxed model is obtained by substituting one aluminum atom by one chromium atom in the beryl structure. The calculated isotropic XANES spectra are quite similar for both structural models. However, the features lying at 5998.5 and 6001.3 eV (called *a* and *b* in Fig. 7) are better represented by the simulation using the relaxed model. In the simulation using the nonrelaxed model, only one feature (called *c* in Fig. 7) is noticeable in the energy range of 5996–6003 eV, instead of two in the experimental spectra. At higher energy, the relaxation effects are still present (for example, around 6025 eV, see feature *d* in Fig. 7) but less obvious. The same behavior is noticed for the dichroic spectra. The agreement between the experimental and the calculated spectra is better when using the relaxed structural model, especially at low energy, where the simulation of the XANES is more subtle.

2. Preedge features

The preedge features contain useful information on the electronic structure around the absorbing atom. The preedge transitions originate from a sum of electric quadrupole $1s \rightarrow 3d$ and of electric dipole $1s \rightarrow p$ transitions. Since the site of the absorbing atom is not centrosymmetric, the *p* orbitals can hybridize with the 3*d* level. The electric dipole and electric quadrupole contributions to the absorbing cross section in the preedge region are represented in Fig. 10. The contributions of spin up and spin down are detailed. The interpretation of the features is possible through group theory in the monoelectronic approach, using the character tables of the D_3 and O_h symmetry groups from Ref. 43. The 1*s* initial state is totally symmetric ($\Gamma_i = a_1$) so that the irreducible representation (called Γ) associated with the various transitions, given by $\Gamma_f \otimes \Gamma_{\mathcal{O}} \otimes \Gamma_i$, depends on the symmetries $\Gamma_{\mathcal{O}}$ of the transition operator $\mathcal{O}$ and of the symmetry Γ_f of the final state (*p* or *d*). A transition is allowed if it has the symmetry of a scalar, i.e., if it transforms like the totally symmetric irreducible representation. Before going further in the interpretation of the preedge features, it is useful to know the symmetry of the *p* and *d* orbitals. The *p* orbitals belong to the $t_{1u}(O_h)$ irreducible representation within octahedral symmetry, and then to the $e(D_3)$ and $a_2(D_3)$ when the O_h symmetry is lowered to D_3. The *d* orbitals belong to the $t_{2g}(O_h)$ and $e_g(O_h)$ irreducible representations within octahedral symmetry. When lowering the symmetry to D_3, the $t_{2g}(O_h)$ irreducible representation is split into the $e(D_3)$ and $a_1(D_3)$ irreducible representations, while $e_g(O_h)$ becomes $e(D_3)$.

In the case of pure electric dipole transitions ($1s \rightarrow p$), the irreducible representation of the transition operator $\mathcal{O}$ depends on the angle between the polarization of x ray and the optical axis of the sample. When the preedge is collected with the polarization of x ray parallel to the optical axis of the sample, $\mathcal{O}$ belongs to the $a_2(D_3)$ irreducible representation. Allowed transitions occur toward final states with the $a_2(D_3)$ symmetry. Therefore, only the p_z state could be probed (the *z* direction is the *c* axis of the cell and corresponds to the optical axis of the sample). However, hybridization between the p_z state and 3*d* states are forbidden by symmetry considerations for the D_3 point group. No transition is then expected on the electric dipole transitions when the polarization of x ray is parallel to the optical axis of the sample. It is in agreement with the simulation of the preedge, which does not exhibit any feature for the dipole contribution (called E1) on the left side of Fig. 10. When the preedge is collected with the polarization of x ray perpendicular to the optical axis of the sample, $\mathcal{O}$ belongs to the $e(D_3)$ irreducible representation. Allowed transitions occur toward states with the $e(D_3)$ symmetry. On the right side of Fig. 10, the intensities of the features corresponding to the electric dipole transitions (called E1) are very weak. It seems then that the hybridization between the *p* and *d* states of chromium in emerald is small. It is quite different from what happens in ruby,[58] where the intensity of the calculated electric dipole transitions are stronger. In fact, the distortion of the chromium site in ruby is larger than in emerald. The symmetry of the chromium site in ruby is C_3 and favors *p*-*d* hybridization.

In the case of pure electric quadrupole transitions ($1s \rightarrow 3d$), the transition operator $\mathcal{O}$ transforms like the $e(D_3)$ irreducible representation, whatever the angle between the polarization of x ray and the optical axis of the sample if the propagation vector of x ray stays perpendicular to the optical axis of the sample. The probed final states have to belong then to the $e(D_3)$ irreducible representation. The simulation of the preedge (Fig. 10) determines the contributions from spin up ($\uparrow$) and spin down ($\downarrow$) final states. Since the $e^{\uparrow}(D_3)$ states coming from the $t_{2g}^{\uparrow}(O_h)$ states are occupied, the 1*s*

transitions toward $3d^{\uparrow}$ states affect only the $e^{\uparrow}(D_3)$ states coming from the $e_g^{\uparrow}(O_h)$ states. Only one feature is noticeable for the electric quadrupole contributions on the calculated spectra. Concerning the $1s$ transitions toward $3d^{\downarrow}$ states, transitions toward $e^{\downarrow}$ coming from both $t_{2g}^{\downarrow}(O_h)$ and $e_g^{\downarrow}(O_h)$ states are allowed. Two features are then noticeable for the electric quadrupolar contributions on the calculated spectra. The energy difference (1.3 eV) between these two features gives an idea of the $t_{2g}^{\downarrow}(O_h)$-$e_g^{\downarrow}(O_h)$ splitting due to the crystal field. This can be compared to optical measurements of the crystal field, which is 2.00 eV,[59] though one should keep in mind that in the monoelectronic picture, the crystal field band at 2.00 eV is associated with spin up levels.

IV. CONCLUSIONS

The crystallographic and electronic structures around chromium in emerald has been determined by XAS. The Cr-O distance (1.97_5 Å) of the coordination shell of chromium in emerald is larger than the Al-O distance (1.90 Å) of the coordination shell of aluminum in beryl. However, it is very similar to the mean Cr-O distance of the coordination shell of chromium in ruby (1.96_5 Å) and also in eskolaite Cr_2O_3 (1.98 Å).[4,5] As a consequence, the slight difference in the Cr-O distance between ruby and emerald (less than 0.3%) cannot by itself explain the difference of color between the two minerals. For ruby, the crystal field $10Dq$ is 2.23 eV and the Racah B parameter is 0.080 eV; for emerald, the crystal field $10Dq$ is 2.00 eV and the Racah B parameter is 0.097 eV. The variation of the crystal field between ruby and emerald is then less than 11%.[2,7,59–63] The general formula $10Dq=KR^n$ where K accounts for the electronic charge on the ligands and the radial integral of d orbitals and where $n=5$ within the point charge model scheme of the crystal field theory cannot make the connection between the observed $10Dq$ value and the difference of mean Cr-O distance.[8,64]

In a previous work[6] dealing with the solid solution $Al_{2-x}Cr_xO_3$, we showed that the color of the crystals could not be easily related to the mean Cr-O distance. We invoked the presence of Cr-Cr coupling that were likely to complicate the picture of an isolated Cr paramagnetic impurity. In a recent series of papers, Moreno *et al.*[57,59] have attributed the $10Dq$ variation to the tensor properties associated with the point group symmetry of the chromium site. This argument was mentioned to explain the difference between red ruby ($Al_2O_3:Cr^{3+}$) and green chromic emerald ($Be_3Si_6Al_2O_{18}:Cr^{3+}$). To separate the influence of Cr-Cr interaction from symmetry consideration, one should study highly symmetric crystals with variable chromium concentration.

ACKNOWLEDGMENTS

We are very grateful to Julian Ledieu for a critical reading of the manuscript. The synthetic single crystal of chromium doped beryl was kindly provided by A. Cheilletz. We are glad to thank Steven I. Dutch who allowed us to use his figures of the beryl structure. We wish to acknowledge the computational support of the French Institut du Développement et de Recherche en Informatique Scientifique in Orsay (Project Nos. 1261 and 72015), where all the calculations of this study were carried out.

[1] L. E. Orgel, Nature (London) **179**, 1348 (1957).
[2] K. Nassau, *The Physics and Chemistry of Color* (Wiley Interscience, New York, 1983).
[3] R. Tilley, *Color and the Optical Properties of Materials* (Wiley, New York, 2000).
[4] E. Gaudry, A. Kiratisin, P. Sainctavit, C. Brouder, F. Mauri, A. Ramos, A. Rogalev, and J. Goulon, Phys. Rev. B **67**, 094108 (2003).
[5] E. Gaudry, D. Cabaret, P. Sainctavit, C. Brouder, F. Mauri, A. Rogalev, and J. Goulon, J. Phys.: Condens. Matter **17**, 5467 (2005).
[6] E. Gaudry, P. Sainctavit, F. Juillot, F. Bondioli, P. Ohresser, and I. Letard, Phys. Chem. Miner. **32**, 710 (2006).
[7] D. S. McClure, J. Chem. Phys. **36**, 2757 (1962).
[8] K. Langer, Z. Kristallogr. **216**, 87 (2001).
[9] R. Büscher, K. P. Such, and G. Lehmann, Phys. Chem. Miner. **14**, 553 (1987).
[10] Z. Wen-Chen, Physica B **245**, 119 (1998).
[11] J. W. McCauley and G. V. Gibbs, Z. Kristallogr., **135**, 453 (1972).
[12] S. C. Moss and R. E. Newnham, Z. Kristallogr. **120**, 359 (1964).
[13] S. Emura, H. Maeda, Y. Kuroda, and T. Murata, *Proceedings of the Seventh International Conference on X-Ray Absorption Fine Structure, Kobe, Japan, 1992* [Jpn. J. Appl. Phys., Part 1 **32**, 734 (1993)].
[14] C. Verdozzi, D. R. Jennison, P. A. Schultz, M. P. Sears, J. C. Barbour, and B. G. Potter, Phys. Rev. Lett. **80**, 5615 (1998).
[15] L. A. Errico, M. Renteria, and H. M. Petrilli, Phys. Rev. B **75**, 155209 (2007).
[16] G. A. Waychunas, Am. Mineral. **72**, 89 (1987).
[17] G. A. Waychunas, M. Apted, and G. Brown, Phys. Chem. Miner. **10**, 1 (1983).
[18] A. Manceau, A. I. Gorshkov, and V. A. Drits, Am. Mineral. **77**, 1133 (1992).
[19] M. Taillefumier, D. Cabaret, A.-M. Flank, and F. Mauri, Phys. Rev. B **66**, 195107 (2002).
[20] *Cristallographie, ou Description des Formes…du Règne Minéral*, 2nd ed. edited by J. R. de l'Isle (L'imprimerie de Monsieur, Paris, 1783), Vol. 4.
[21] R.-J. Haüy, *Traité de Cristallographie* (Bachelier et Huzard, Paris, 1822), Vol. 2.
[22] *International Tables for Crystallography*, edited by T. Hahn (The International Union of Crystallography, Dordrecht, 1995), Vol. A.
[23] J. Cassedanne and J.-M. LeCléac'h, Minéraux et fossiles **5** (1997).
[24] G. V. Gibbs, D. W. Breck, and E. P. Meagher, Lithos **1**, 275

(1968).
[25] B. Morosin, Acta Crystallogr., Sect. B: Struct. Crystallogr. Cryst. Chem. **28**, 1899 (1972).
[26] J. Goulon, A. Rogalev, C. Gauthier, C. Goulon-Ginet, S. Paste, R. Signorato, C. Neumann, L. Varga, and C. Malgrange, J. Synchrotron Radiat. **5**, 232 (1998).
[27] A. Rogalev, J. Goulon, C. Goulon-Ginet, and C. Malgrange, in *Magnetism and Synchrotron Radiation*, edited by E. Beaurepaire, F. Scheurer, G. Krill, and J.-K. Kappler (Springer, New York, 2001), pp. 60–86.
[28] J. Goulon *et al.*, J. Synchrotron Radiat. **12**, 57 (2005).
[29] C. Brouder, D. Cabaret, P. Sainctavit, A. Kiratisin, J. Goulon, and A. Rogalev, *Proceedings of the 14th International Conference on Defects in Insulating Materials (ICDIM), Johannesburg* [Radiat. Eff. Defects Solids II, 89 (2001)].
[30] E. Gaudry, Ph.D. thesis, Université Pierre et Marie Curie (Paris 6), 2004; http://tel.archives-ouvertes.fr
[31] M. Winterer, J. Phys. IV **7**, 243 (1997).
[32] D. Bonnin, G. Calas, H. Suquet, and H. Pezerat, Phys. Chem. Miner. **12**, 55 (1985).
[33] *X-ray Absorption: Principles, Applications, Techniques of EXAFS, SEXAFS and XANES*, edited by D. C. Koningsberger and R. Prins (Wiley, New York, 1988).
[34] A. L. Ankudinov, B. Ravel, J. J. Rehr, and S. D. Conradson, Phys. Rev. B **58**, 7565 (1998).
[35] FEFF project, Department of Physics, University of Washington, Seattle, WA 98195-1560 (copyright 1992–2006); for more information see http://leonardo.phys.washington.edu/feff/
[36] B. K. Teo, *EXAFS: Basic Principles and Data Analysis* (Springer, New York, 1985).
[37] R. Car and M. Parrinello, Phys. Rev. Lett. **55**, 2471 (1985).
[38] J. Hutter, P. Ballone, M. Bernasconi, P. Focher, E. Fois, S. Goedecker, M. Parrinello, and M. Tuckerman, Stuttgart and IBM Research, 1996.
[39] CPMD V3.7, Copyright IBM Corp. 1990–2003 (Copyright MPI für Festkörperforschung Stuttgart 1997–2001); for more information see http://http://www.cpmd.org
[40] S. Goedecker, M. Teter, and J. Hutter, Phys. Rev. B **54**, 1703 (1996).
[41] N. Troullier and J. L. Martins, Phys. Rev. B **43**, 1993 (1991).
[42] L. Kleinman and D. M. Bylander, Phys. Rev. Lett. **48**, 1425 (1982).
[43] A. B. P. Lever, *Inorganic Electronic Spectroscopy* (Elsevier, New York, 1984).
[44] Calculations were performed with PARATEC (PARAllel Total Energy Code) by B. Pfrommer, D. Raczkowski, A. Canning, S. G. Louie, F. Mauri, M. Cote, Y. Yoon, Ch. Pickard, and P. Haynes, Lawrence Berkeley National Laboratory; for more information see http://www.nersc.gov/projects/paratec
[45] D. Cabaret, E. Gaudry, M. Taillefumier, P. Sainctavit, and F. Mauri, Phys. Scr., T **T115**, 131 (2005).
[46] P. E. Blöchl, Phys. Rev. B **50**, 17953 (1994).
[47] R. Haydock, V. Heine, and J. M. Kelly, J. Phys. C **5**, 2845 (1972).
[48] R. Haydock, V. Heine, and J. M. Kelly, J. Phys. C **8**, 2591 (1975).
[49] H. J. Monkhorst and J. D. Pack, Phys. Rev. B **13**, 5188 (1976).
[50] J. Kokubun, K. Ishida, D. Cabaret, F. Mauri, R. V. Vedrinskii, V. L. Kraizman, A. A. Novakovich, E. V. Krivitskii, and V. E. Dmitrienko, Phys. Rev. B **69**, 245103 (2004).
[51] K. Eigenmann, K. Kurtz, and H. H. Günthard, Helv. Phys. Acta **45**, 452 (1972).
[52] R. D. Shannon, Acta Crystallogr., Sect. A: Cryst. Phys., Diffr., Theor. Gen. Crystallogr. **A32**, 751 (1976).
[53] L. A. Errico, G. Fabricius, M. Renteria, P. de la Presa, and M. Forker, Phys. Rev. Lett. **89**, 055503 (2002).
[54] A. Juhin, G. Calas, D. Cabaret, L. Galoisy, and J.-L. Hazemann, Phys. Rev. B **76**, 054105 (2007).
[55] W. B. Pearson, *Structure Reports* (International Union of Crystallography, Utrecht, 1962), Vol. 27.
[56] T. Yamanaka and Y. Takeuchi, Z. Kristallogr. **165**, 65 (1983).
[57] M. Moreno, M. T. Barriuso, J. A. Aramburu, and P. G.-F. ans J. M. Garcia-Lastra, J. Phys.: Condens. Matter **18**, R315 (2006).
[58] E. Gaudry, D. Cabaret, P. Sainctavit, C. Brouder, F. Mauri, A. Rogalev, and J. Goulon, Phys. Scr., T **T115**, 191 (2005).
[59] J. M. Garcia-Lastra, M. T. Barriuso, J. A. Aramburu, and M. Moreno, Phys. Rev. B **72**, 113104 (2005).
[60] C. P. Poole, J. Phys. Chem. Solids **25**, 1169 (1964).
[61] D. M. Dood, J. Chem. Phys. **42**, 3404 (1965).
[62] B. Di Bartolo and G. Armagan, *Spectroscopy of Solid-State Laser-Type Materials*, Ettore Majorana International Science Series (Springer, New York, 1987).
[63] R. G. Burns, *Mineralogical Applications of Crystal Field Theory*, Cambridge Topics in Mineral Physics and Chemistry, Vol. 5, 2nd ed. (Cambridge University Press, Cambridge, 1993).
[64] T. Dunn, D. S. McClure, and R. G. Pearson, *Some Aspects of Crystal Field Theory* (Harper and Row, New York, 1965).